



# Efficiency and coherence preservation studies of Be refractive lenses for XFEL application

Tomasz Kolodziej,<sup>a\*</sup> Stanislav Stoupin,<sup>a‡</sup> Walan Grizolli,<sup>a</sup> Jacek Krzywinski,<sup>c</sup> Xianbo Shi,<sup>a</sup> Kwang-Je Kim,<sup>a</sup> Jun Qian,<sup>a</sup> Lahsen Assoufid<sup>a</sup> and Yuri Shvyd'ko<sup>a</sup>

<sup>a</sup>Advanced Photon Source, Argonne National Laboratory, Lemont, IL 60439, USA, and <sup>c</sup>Linac Coherent Light Source, SLAC National Accelerator Laboratory, Menlo Park, CA 94025, USA. \*Correspondence e-mail: kolodziej@aps.anl.gov

Received 7 August 2017

Accepted 26 November 2017

Edited by M. Yabashi, RIKEN SPring-8 Center, Japan

‡ Present address: Cornell High Energy Synchrotron Source, Cornell University, Ithaca, NY 14853, USA.

**Keywords:** X-rays; X-ray focusing; X-ray optics; refractive lenses.

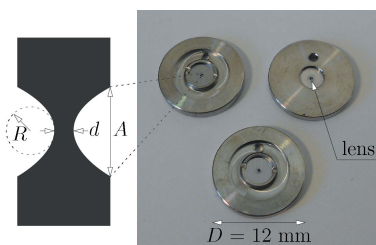
Performance tests of parabolic beryllium refractive lenses, considered as X-ray focusing elements in the future X-ray free-electron laser oscillator (XFEL), are reported. Single and double refractive lenses were subject to X-ray tests, which included: surface profile, transmissivity measurements, imaging capabilities and wavefront distortion with grating interferometry. Optical metrology revealed that surface profiles were close to the design specification in terms of the figure and roughness. The transmissivity of the lenses is >94% at 8 keV and >98% at 14.4 and 18 keV. These values are close to the theoretical values of ideal lenses. Images of the bending-magnet source obtained with the lenses were close to the expected ones and did not show any significant distortion. Grating interferometry revealed that the possible wavefront distortions produced by surface and bulk lens imperfections were on the level of  $\sim \lambda/60$  for 8 keV photons. Thus the Be lenses can be successfully used as focusing and beam collimating elements in the XFEL.

## 1. Introduction

Contemporary experimental science is being shaped by the constant advancement in the development of accelerator-based X-ray sources. Diffraction-limited synchrotron radiation sources, X-ray free-electron lasers (XFELs) and X-ray free-electron laser oscillators (XFELOs) promise to deliver X-ray beams of a high degree of coherence and high brilliance and power over a wide spectral range. This calls for the development of highly transparent and coherence-preserving optics. In XFEL cavities in particular, focusing elements of high transmissivity are necessary to control the beam profile (Kim *et al.*, 2008; Kim & Shvyd'ko, 2009).

Possible focusing elements of hard X-rays include Fresnel zone plates, multilayer Laue (MLL) devices (Morgan *et al.*, 2015) and curved grazing mirrors in Kirkpatrick–Baez configuration. However, the efficiency of Fresnel zone-plates and MLLs is too low. A curved grazing mirror should work but is bulky and expensive. Here we study parabolic compound refractive lenses (CRLs) as a compact and simple-to-implementation option. Note that the efficiency of a CRL consisting of many units for a short focal length is usually very small, less than 50%. For the XFEL application, however, the required focal length is typically about 50 m or longer. In this case the lens can be made from at most two units with high transmission efficiency.

The first CRLs were in the form of a series of a cylindrical drillings in a metal block made of a light element (*e.g.* Al, Be) in one direction for one-dimensional focusing or two sets of perpendicular drillings for two-dimensional focusing (Snigirev



*et al.*, 1996). The surface profile, of parabolic shape to avoid spherical aberration, was constructed for imaging of the synchrotron undulator source (Lengeler *et al.*, 1999). CRLs have been proven to be applicable in focusing X-rays down to micrometer and nanometer size (Schroer *et al.*, 2005; Schroer & Lengeler, 2005), X-ray microscopy (Bosak *et al.*, 2010; Byelov *et al.*, 2013), beam conditioning (Chumakov *et al.*, 2000), monochromatization (Vaughan *et al.*, 2011), harmonic rejection (Polikarpov *et al.*, 2014) and many more.

Refractive lenses can be manufactured from a variety of materials (Roth *et al.*, 2017; Shvyd'ko *et al.*, 2017; Terentyev *et al.*, 2015). Beryllium, as one of the lightest elements, is being widely used in X-ray optics due to its high transparency to X-rays, and also for manufacturing the CRLs (Lengeler *et al.*, 1999, 2005). CRLs at existing beamlines have been mostly used for focusing the X-ray beams to tight focal spots; thus they are stacks of a large numbers of lenses. For the XFEL's purpose, however, the focal length could be rather long, in the range of several tens of meters. On the other hand, the highest transmissivity and minimal wavefront perturbation is required. In this paper we study whether single or double beryllium lenses can satisfy the XFEL requirements.

## 2. Metrology

### 2.1. Tested lenses

A schematic drawing of the biconcave parabolic Be lens is presented in Fig. 1(a). The shape of the lens surface is a paraboloid obtained by revolving the  $x^2/2R$  curve around its axis, where  $R$  is the surface radius of curvature,  $A$  is the geometrical aperture of the lens, and  $d$  is the minimum wall thickness between two interfaces. The lenses, manufactured from beryllium of IF-1 grade, used for tests in the presented work are shown in Figs. 1(b)–1(d). Design specifications of the inspected lenses #1 and #2 are as follows: radius of curvature  $R = 100 \mu\text{m}$ , geometrical aperture  $A = 600 \mu\text{m}$ , surface microroughness  $\sigma = 100 \text{ nm}$  (RMS) and minimum thickness

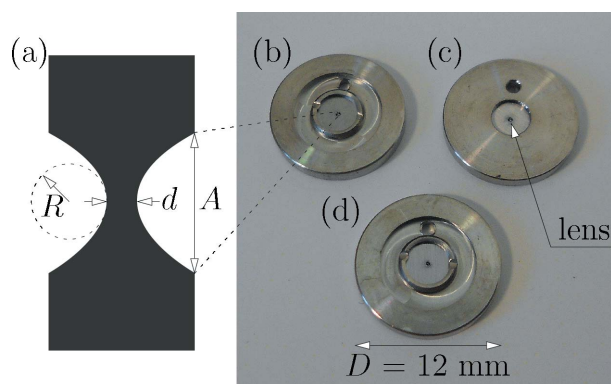


**Figure 1**  
(a) Schematic drawing of the biconcave parabolic Be lens. Photographs of the inspected lenses: (b) Lens #1 ( $R = 100 \mu\text{m}$ ), face 1. (c) Lens #2 ( $R = 100 \mu\text{m}$ ), face 2. (d) Lens #3 ( $R = 50 \mu\text{m}$ ), face 1. Small indentations in the center of the beryllium foils are the actual lenses. The total diameter of the lens with the mounting disk is 12 mm. See text for details.

**Table 1**

Nominal and measured values for the radii of curvature ( $R$ ) and surface microroughnesses ( $\sigma$ , RMS) for each side of the inspected lenses.

Lens	Face	$R_{\text{nom}}$ ( $\mu\text{m}$ )	$\sigma_{\text{nom}}$ (nm)	$R_{\text{meas}}$ ( $\mu\text{m}$ )	$\sigma_{\text{meas}}$ (nm)
#1	1	100	100	109	93
	2			101	81
#2	1	100	100	99	122
	2			103	76
#3	1	50	100	50	100
	2			50	130

$d = 32.5 \mu\text{m}$ . Lens #3:  $R = 50 \mu\text{m}$ ,  $A = 400 \mu\text{m}$ ,  $\sigma = 100 \text{ nm}$  (RMS) and  $d = 28 \mu\text{m}$ .

### 2.2. Figure and surface roughness

Optical metrology of the  $R = 100 \mu\text{m}$  Be lenses was performed with the MicroXAM RTS microscope interferometer, and the  $R = 50 \mu\text{m}$  lens was inspected with the NexView interferometer at the Advanced Photon Source (APS) facility. Measurement uncertainty of the surface quality given by the interferometer is of the order of 1 nm. One of the center-line profiles of the surface figure for lens #1, surface 2, is presented in Fig. 2. The profile is a good fit with the parabola  $f(x) = x^2/2R$  with  $R = 101 \mu\text{m}$ , which is very close to the nominal value. One can notice that, after the manufacturing process, the profile of the lens in the bottom part deviates slightly from parabolic (is flatter), which is also observable in the results of the Talbot interferometry (see §2.3 for comparison). The results of the optical metrology of all three lenses are shown in Table 1, where the surface radius and microroughness is measured for the paraboloidal surface in the central 90–100  $\mu\text{m}$  area of lenses #1 and #2, and the central 60  $\mu\text{m}$  of lens #3. In the case of lens #1, face 1, however, the fitted surface radius of curvature exceeds the nominal value by 9%. In other cases the values are very close to the design parameter. Surface microroughness values are in most cases smaller than the specified 100 nm (RMS); only in the case of lens #2, face 1, the measured value is higher from the nominal by 22%, and in lens #3, face 2 by 30%.

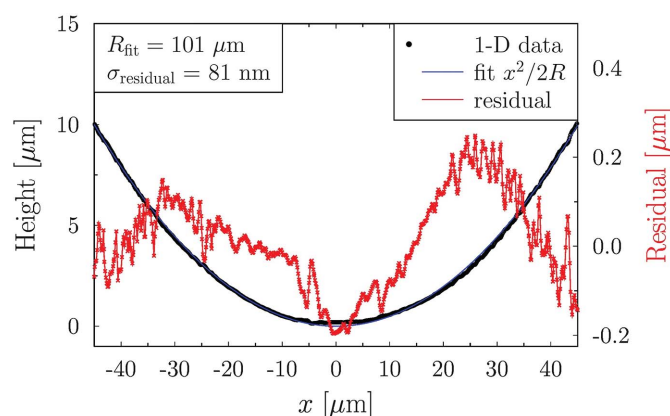


**Figure 2**  
Center-line profile of lens #1, face 2, measured with the MicroXAM RTS microscope interferometer. The red curve represents the residual defined here as (parabolic fit – experimental data).

### 2.3. Talbot interferometry for optical thickness

While visible-light metrology provides the surface profiles of the lenses, single-grating interferometry provides the optical thickness of the lens (Itoh *et al.*, 2011; Wang *et al.*, 2009). This is a critical parameter since the performance of the lens is dictated by the optical path length.

Single-grating interferometry uses the Talbot self-imaging effect (Goodman, 2005) in the X-ray regime to obtain a differential phase contrast image of a sample. By placing a phase object in the beam path, we introduce a phase shift that changes the wavefront and deforms the self-image of the grating. From the deformed self-image we obtain the two-dimensional gradient of the phase shift (differential phase contrast, DPC) (Itoh *et al.*, 2011) caused by the sample. The DPC signal is then used to calculate the phase shift  $\varphi(x, y)$  caused by the object (Frankot & Chellappa, 1988). The phase shift can be interpreted as distortions to the wavefront or be used to retrieve the thickness  $T(x, y)$  of the object by the equation

$$T(x, y) = -\frac{\lambda}{2\pi} \frac{\varphi(x, y)}{\delta(\lambda)}, \quad (1)$$

valid for an homogeneous material of known refractive index  $n(\lambda) = 1 - \delta(\lambda) + i\beta(\lambda)$ , where  $\lambda$  is the wavelength of the radiation and  $\varphi(x, y)$  is the phase shift in radians.

The measurements of the lenses were performed using a portable grating interferometer (Assoufid *et al.*, 2016) at APS beamline 1-BM-B (Macrander *et al.*, 2016). The beamline was tuned at 8 keV photon energy ( $\lambda \simeq 1.55 \text{ \AA}$ ) and the detector has an effective pixel size  $0.65 \mu\text{m} \times 0.65 \mu\text{m}$ . The experiments used a  $\pi/2$  checkerboard phase grating with period  $p_G = 4.8 \mu\text{m}$  to generate the Talbot self-images. The diagonal directions of the checkerboard pattern were aligned in the horizontal and vertical directions to achieve the highest contrast (Marathe *et al.*, 2014). We used the third Talbot distance, determined experimentally at 184 mm. The resulting transverse resolution is defined by the period of the self-image and is equal to  $p_G/\sqrt{2} = 3.4 \mu\text{m}$ . For these conditions, the minimum measurable beryllium thickness is estimated to be  $\sim 50 \text{ nm}$ . A potential source of error is the value of  $\delta$ , which uses tabulated values (Schoonjans *et al.*, 2011) of refractive index and density. For beryllium at 8 keV the tabulated value for  $\delta$  is  $5.327 \times 10^{-6}$ .

We performed two sets of measurements: first a stack of lenses #1 and #2, and then lens #3 individually. It can be shown that the resulting thickness of biconcave parabolic lenses is also described by a parabolic function. The resulting function can be further simplified by assuming that the lens surfaces are perfectly aligned (center of all surfaces in the symmetrical axis of the lens) and that all surfaces have the same curvature radius. In this condition the effective curvature radius  $R_T$  of the thickness profile is equal to the curvature of the surfaces  $R_{\text{surf}}$  divided by the number of curved surfaces  $n_{\text{surf}}$ . This result is also valid for a stack of lenses and therefore, by stacking lenses #1 and #2, we obtain the same effective radius  $R_T = R_{\text{surf}}/n_{\text{surf}} = 25 \mu\text{m}$  as that of lens #3 individually.

**Table 2**  
Results for the profile fittings.

The curvature radii obtained from the fits were multiplied by the number of surfaces in order to compare with the nominal surface radius. The obtained value of the curvature radius is therefore an average of the radius of all the curved surfaces.

Nominal surface radius ( $\mu\text{m}$ )	Average surface radius ( $\mu\text{m}$ )	Residual RMS (nm)	Residual peak-to-valley ( $\mu\text{m}$ )	Direction
50	52.12	231	0.71	Horizontal
50	49.98	244	0.83	Vertical
100	94.92	489	1.64	Horizontal
100	92.64	505	1.74	Vertical

Analogously to the visible-light metrology, we fit a parabolic function to the two central thickness profiles from where we obtain  $R_T$ , shown in Fig. 3 and Table 2. The residuals are obtained from the difference between the best-fit curve and the measured thickness. Further analyses using a two-dimensional fitting is shown in Fig. 4 and Table 3. The statistical errors for the two-dimensional case are slightly higher because the fitted surface assumes the same curvature radius in orthogonal directions (stigmatic). In fact, the higher error values are an indication that the lenses have a small degree of astigmatism, which is also observed in the different values of

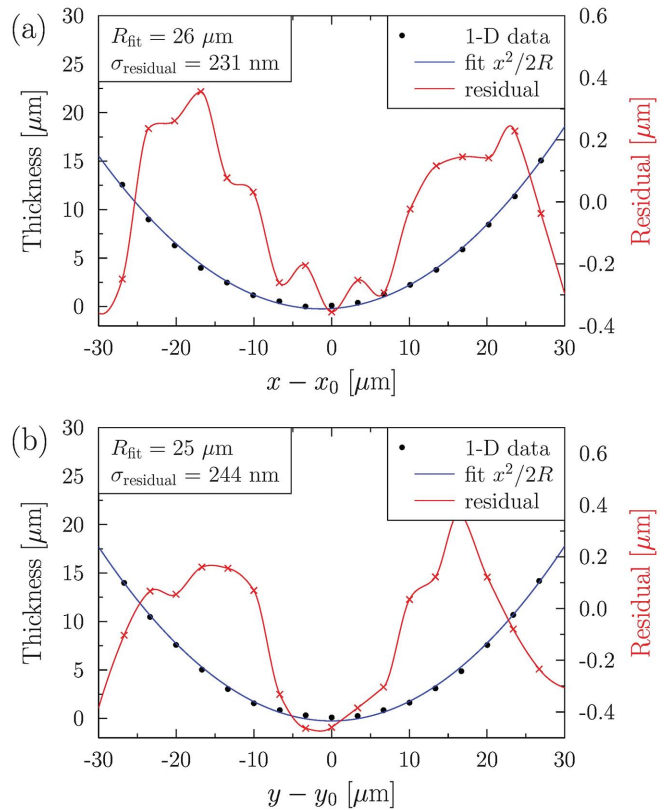


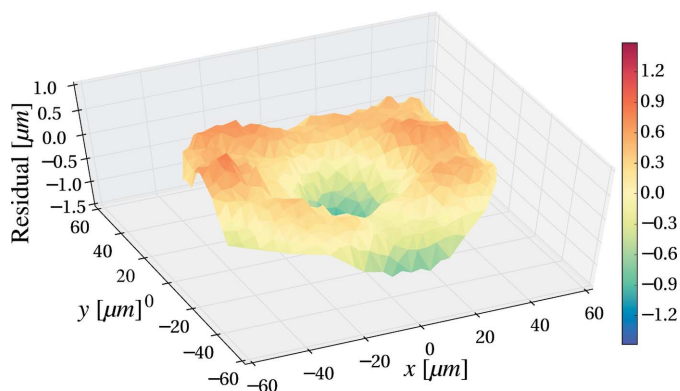
**Figure 3**  
Center-line thickness profiles of lens #3, in (a) the horizontal and (b) the vertical direction. The ideal value for the fitted curvature radius  $R_{\text{fit}}$  is  $25 \mu\text{m}$ , equal to the curvature radius of the surface divided by the number of curved surfaces (two for the  $50 \mu\text{m}$  lens). The residual is defined here as (parabolic fit – experimental data), the same as in Fig 2.

**Table 3**

Results for the surface fitting.

Fitted curvature radii were multiplied by the number of surfaces in order to compare with the nominal surface radius.

Nominal surface radius ( $\mu\text{m}$ )	Average surface radius ( $\mu\text{m}$ )	Residual RMS $\sigma_{\text{thickness}}$ (nm)	Residual peak-to-valley ( $\mu\text{m}$ )	Total surface RMS error $\sigma_T$ (nm)
50	50.68	260	1.15	164
100	96.88	455	2.34	190


**Figure 4**

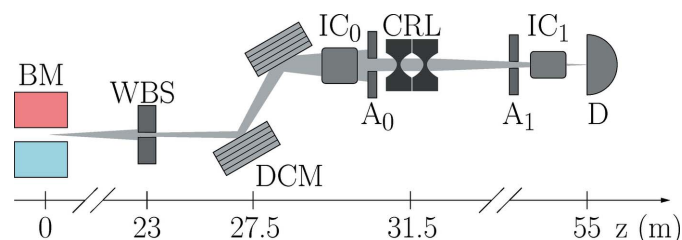
Residual of the stack of lenses #1 and #2. Fitting results are given in Table 3. The curvature radius of the fitting surface is uniform in all directions (that is, it uses a stigmatic surface).

the radii for the orthogonal profiles in Table 2. The obtained values of the curvature radii in Tables 2 and 3 are slightly smaller than the nominal values. Considering that the values obtained for the surface metrology have a very good agreement with the nominal values, these differences are attributed to a small deviation of refractive index from the tabulated values used in equation (1).

### 3. Transmission and imaging

#### 3.1. Layout

X-ray tests of the presented refractive lenses were conducted at beamline 1-BM-B,C of the APS synchrotron radiation facility (Macrander *et al.*, 2016). Experiments were conducted in the near- and far-field. A scheme of the experiment in the far-field is presented in Fig. 5. White beam generated by the bending magnet, of size defined by the white-beam slits, is monochromated by a double-crystal Si(111) monochromator down to a spectral resolution of  $1.5 \times 10^{-4}$ . The beam in front of the refractive lenses is defined by a circular pinhole of diameter  $290 \mu\text{m}$ , or by square slits of changing size. The lenses tested were as follows: a single biconcave lens with  $R = 50 \mu\text{m}$  and two stacked biconcave lenses with  $R = 100 \mu\text{m}$ . This should result in the same focal distance of both lenses for a given photon energy, since the focal length can be calculated using the formula  $f = R/2N\delta$  [see Lengeler *et al.* (1999) for reference]. To avoid any possible


**Figure 5**

Simplified scheme of the experiment at 1-BM-B,C (APS). BM: bending magnet. WBS: white-beam slits. DCM: Si(111) double-crystal monochromator. IC<sub>0</sub>: ionization chamber (intensity monitor). A<sub>0</sub>: beam-defining aperture. CRL: compound refractive lens. A<sub>1</sub>: second aperture. IC<sub>1</sub>: second ionization chamber. D: detector (digital X-ray area detector or PIN diode). See text for details.

beryllium oxidation effects while exposed to X-rays, the lenses were enclosed in a specially designed casing under the flow of gaseous helium.

#### 3.2. Lenses transmissivity

Experiments were conducted in both the near- and far-field. For the far-field transmissivity measurement, the flux was measured using a PIN diode detector with the lens in ( $I_1$ ) and out of ( $I_0$ ) the beam, including the signal from the detector without the beam on (background  $B$ ). To avoid errors connected to the storage-ring current variations, normalization of the measurements with respect to the incoming beam intensity was used (measured by the ionization chamber placed in front of the experiment, serving as the intensity monitor). The transmissivity is then defined as  $T = [(I_1 - B)/I_{\text{mon}1}]/[(I_0 - B)/I_{\text{mon}0}]$ . The near-field transmissivity of the lenses was measured at three different photon energies: 8 keV, 14.4 keV and 18 keV, with a circular pinhole of  $290 \mu\text{m}$  diameter aligned in front of the lens. A PIN diode was placed 10 cm downstream from the lenses. The far-field transmissivity was measured at a photon energy of 14.4 keV, with the detector placed 23.5 m downstream of the lenses, with square slits of variable size defining the beam. In the far-field an additional  $1 \text{ mm} \times 1 \text{ mm}$  square aperture was placed in front of the detector, to reject the photons scattered out of the focusing direction due to small-angle scattering on the surface microroughness and grain boundaries.

The results of the transmissivity measurement are shown in Tables 4 and 5. The experimental data are compared with theoretical values of the transmissivity for ideal lenses, calculated with the analytical formula given by Lengeler *et al.* (1999), for circular pinhole and square slits, respectively. No effect of the small-angle scattering from surface imperfections and grain boundaries is included in this calculation. Additionally, the theoretical transmissivities were calculated with the atomic scattering form factor correction of beryllium taken from three widely used databases (Henke *et al.*, 1993; Chantler *et al.*, 2017; Kissel *et al.*, 1995), for comparison. Only at the lowest energy,  $E = 8 \text{ keV}$ , can one notice a  $\sim 0.5\%$  difference in the theoretical transmission between these sources.

**Table 4**

Transmission of the lenses in the near-field as a function of photon energy  $E$ , with a 290  $\mu\text{m}$  circular pinhole aligned in front of the lenses.

Experimental data are compared with the theoretical transmissivity of Be lenses with zero roughness of the parabolic profile assumed. Absorption coefficients are calculated with atomic scattering form factor corrections taken from Henke *et al.* (1993) (H), Chantler *et al.* (2017) (N) and Kissel *et al.* (1995) (K). See text for details.

$E$ (keV)	$T_{\text{meas}}$ (%)	$T_{\text{theor}}$ (H) (%)	$T_{\text{theor}}$ (N) (%)	$T_{\text{theor}}$ (K) (%)
$1 \times 50 \mu\text{m}$				
8	95.15	96.06	96.55	96.13
14.4	98.39	99.42	99.49	99.44
18	98.86	99.72	99.76	99.73
$2 \times 100 \mu\text{m}$				
8	94.23	95.58	96.12	95.71
14.4	98.23	99.35	99.42	99.37
18	98.71	99.69	99.73	99.70

**Table 5**

Transmission of the lenses in the far-field as a function of the size of the square slits in front of the lens, at photon energy  $E = 14.4$  keV, compared with theoretical values of transmissivity, as in Table 4.

$a$ ( $\mu\text{m}$ )	$T_{\text{meas}}$ (%)	$T_{\text{theor}}$ (H) (%)	$T_{\text{theor}}$ (N) (%)	$T_{\text{theor}}$ (K) (%)
$1 \times 50 \mu\text{m}$				
100	99.67	99.85	99.86	99.85
150	99.68	99.75	99.77	99.76
170	99.61	99.70	99.73	99.71
200	99.63	99.61	99.65	99.62
$2 \times 100 \mu\text{m}$				
100	98.92	99.77	99.80	99.78
150	98.76	99.67	99.71	99.68
170	98.79	99.62	99.66	99.64
200	98.65	99.53	99.59	99.55

### 3.3. Imaging quality

The imaging quality of the Be lenses was tested by imaging the bending-magnet source of beamline 1-BM of the APS facility. The nominal source size at 1-BM is 200  $\mu\text{m} \times 71 \mu\text{m}$  (horizontal  $\times$  vertical, FWHM). Lenses were placed  $p = 31.5$  m downstream from the source, and the detector was 55 m from the source ( $q = 23.5$  m from the lenses). In Table 6 the dependence of the image size on the photon energy, obtained with two stacked  $R = 100 \mu\text{m}$  lenses, is presented. The smallest and sharpest image was found for  $E = 13.65$  keV. The same dependence was found for a single  $R = 50 \mu\text{m}$  lens. The image obtained with a single  $R = 50 \mu\text{m}$  lens at 13.65 keV is presented in Fig. 6(a) together with the horizontal [Fig. 6(b)] and vertical [Fig. 6(c)] profiles and widths as fitted with a Gaussian curve. The observable inclination of the image is in agreement with the inclination of the source due to vertical dispersion in the magnetic lattice of the storage ring.

### 3.4. Discussion

Metrological inspection of the commercially available beryllium lenses for synchrotron radiation showed that they are of an excellent quality and meet the design specifications.

**Table 6**

Image size (horizontal and vertical full widths) dependency on the photon energy for the double  $R = 100 \mu\text{m}$  CRL measured with the area detector (see text for details).

$E$ (keV)	13.45	13.55	13.65	13.8	14.4
$\Delta_x$ ( $\mu\text{m}$ )	179	178	172	178	179
$\Delta_y$ ( $\mu\text{m}$ )	65	64	61	63	70

The radius of curvature in the central 100  $\mu\text{m}$  area does not deviate from the nominal; in the single case (lens #1, face 1), the maximal deviation is 9%. The measured surface micro-roughness of the tested lenses exhibits deviations from nominal values by 20–30% in extreme cases; however, the average value of the roughness standard deviation is very close to the specified  $\sigma = 100$  nm.

In order to compare the surface and the thickness root-mean-square errors (RMS),  $\sigma_{\text{surf}}$  and  $\sigma_{\text{thickness}}$ , respectively, one could sum the experimental residual curves from the surface metrology and then calculate the RMS value. However, the measurement of the surface lacks an absolute reference, and it is not possible to know the displacement in the transverse direction between the experimental curves. Alternatively, we simply assumed that the individual surface errors  $\sigma_{\text{surf}_i}$  sum as

$$\sigma_T^2 = \sum_i^{n_{\text{surf}}} \sigma_{\text{surf}_i}^2, \quad (2)$$

where  $\sigma_T$  is the total error due to the surface imperfections and  $i$  is a label index for each of the  $n_{\text{surf}}$  curved surfaces. In Table 3 we show the values of  $\sigma_T$  obtained by applying equation (2) to the values of Table 1. Comparing these values with  $\sigma_{\text{thickness}}$ , we note that the values obtained from grating interferometry can be more than two times higher. This means that the variations in the bulk of the lenses have comparable magnitude with the surface errors of the lenses. The biggest

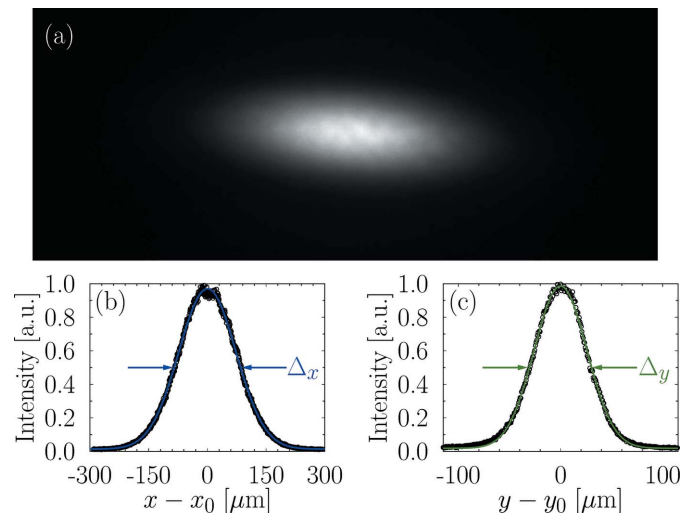


**Figure 6**

(a) Image of the bending-magnet source obtained with a single 50  $\mu\text{m}$  lens at  $E = 13.65$  keV, for distance  $q = 23.5$  m downstream of the lens. Horizontal (b) and vertical (c) profiles of the image are presented. The solid blue (b) and green (c) lines are Gaussian fits to the experimental data. Measured widths are:  $\Delta_x = 172 \mu\text{m}$ ,  $\Delta_y = 61 \mu\text{m}$ .

RMS value in Table 3 is  $\sigma_{\text{thickness}} = 455 \text{ nm}$ , which is equivalent to a wavefront error of  $\sim \lambda/60$ .

In order to evaluate the performance of the lenses as focusing elements in the XFEL, simulations based on wavefront propagation need to be performed. Since the full XFEL simulation with the measured CRL profile is time-consuming, we simplified the computation by neglecting the FEL gain except for restoring the loss of the intensity. In general, an optical cavity consisting of mirrors and lenses has a set of eigen-modes, even if the profiles of the optical elements are not perfect. These modes can be found by the Fox–Li method (Fox & Li, 1961; Siegman, 1986). Thus, we simulated a Gaussian beam iteratively passing through a lens multiple times to obtain its fundamental mode.

The initial Gaussian beam has a  $\sigma$  size of  $10.2 \mu\text{m}$  at  $14.4 \text{ keV}$ . The source-to-lens and lens-to-image distances are both  $13.7 \text{ m}$ . Simulations were performed for both an ideal parabolic lens of  $R = 50 \mu\text{m}$  and lens #3 with the measured thickness profile using Talbot interferometry. When the ideal parabolic lens is used, the wavefield distribution remains the same to the source with only a small reduction of the amplitude after each pass. On the other hand, the wavefield distribution through lens #3 fluctuates for a few thousand passes before reaching its steady state, which will be the fundamental mode. After 10000 passes, the beam size fluctuation is less than 0.35%. Fig. 7 shows the simulated beam intensity profile after 10000 passes of each lens. The beam profile through the ideal lens remains identical to that of the source. The beam profiles through lens #3 are 6.7% and 7.6% wider than the source in the horizontal and vertical directions, respectively. Although these changes can reduce the overlap with the electron beam, the effect on the XFEL performance is expected to be marginally small since the mode will be re-distributed due to the FEL gain. Also, we expect the approach to a steady state will occur well before 10000 passes due to the FEL gain and the filtering of the Bragg mirrors. We plan to perform a more realistic simulation of the XFEL start-up to confirm these expectations. One should note that corrective lenses can also

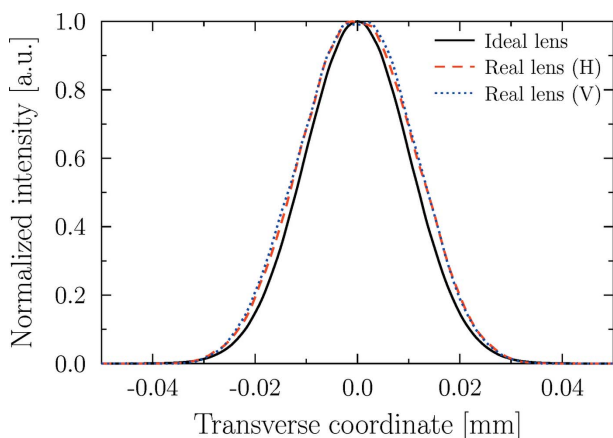


**Figure 7**  
Simulated beam profiles after 10000 passes through an ideal parabolic lens (solid line) and lens #3. The FWHM of the profiles are  $24 \mu\text{m}$ ,  $25.6 \mu\text{m}$  and  $25.8 \mu\text{m}$  for the ideal lens (both directions), and lens #3 in the horizontal and vertical directions, respectively.

**Table 7**  
Values of the theoretical transmissivity for a  $2 \times 100 \mu\text{m}$  CRL for  $0 \text{ nm}$  and  $100 \text{ nm}$  microroughness (RMS).

$E$ (keV)	$T_{\sigma=0\text{nm}}$ (%)	$T_{\sigma=100\text{nm}}$ (%)
8	95.58	95.39
14.4	99.35	99.29
18	99.69	99.65

be used to reduce the errors of a stack of lenses (Seiboth *et al.*, 2017).

The efficiency of the lenses was first tested by measuring the transmissivity in the near-field at three different photon energies:  $8 \text{ keV}$ ,  $14.4 \text{ keV}$  and  $18 \text{ keV}$ . The results are compared with theoretical values of transmission calculated with zero surface roughness assumed (see Table 4). There is a systematic difference in the measured transmissivity of the order of  $\sim 1\%$  lower than calculated for the ideal lens. The difference may be due to the slightly higher thickness than the ideal minimal  $d = 30 \mu\text{m}$  given in the specification, and small-angle scattering on the surface roughness. For a double lens the difference is slightly higher, especially at  $8 \text{ keV}$  ( $\sim 1.5\%$ ), which may be due to the misalignment of the centers (stacking error). The dependence of the transmission for photon energy  $14.4 \text{ keV}$  measured in the far-field on the size of the square slits in front of the lenses is shown in Table 5. The observable tendency for a single lens is as follows: the larger the slit size, the smaller the difference between the experimental and theoretical value that is noticed. The biggest difference of  $0.2\%$  is measured for the smallest slit size of  $100 \mu\text{m} \times 100 \mu\text{m}$ . For the double  $100 \mu\text{m}$  lens, the measured difference is rather constant, on the level of  $0.8\%$ . For stacked lenses, the difference can be caused by stacking errors. The possible impact of the microroughness on the  $2 \times 100 \mu\text{m}$  lens transmissivity is presented in Table 7 for  $\sigma = 0 \text{ nm}$  and  $\sigma = 100 \text{ nm}$ . The roughness impact on the transmission was calculated according to the procedure given by Lengeler *et al.* (1999). One can see that for  $8 \text{ keV}$  the difference is smaller than  $0.2\%$ , and for  $14.4 \text{ keV}$  and  $18 \text{ keV}$  the differences are smaller than  $0.1\%$ , thus the measurable transmissivity is decreased by the coexistence of more factors, as mentioned above.

For the presented experimental conditions ( $p = 31.5 \text{ m}$ ,  $q = 23.5 \text{ m}$ ), a sharp image of the source should be obtained while the focal length  $f = 13.46 \text{ m}$ . This focal length corresponds to a photon energy of  $13.55 \text{ keV}$  for the ideal lens. From the demagnification ratio the expected image size is  $q/p$  times smaller than the source:  $149 \mu\text{m} \times 53 \mu\text{m}$  (FWHM). The best obtained image size is  $172 \mu\text{m} \times 61 \mu\text{m}$  at  $13.65 \text{ keV}$  (the focal length for this energy is  $13.66 \text{ m}$ ). The best image size calculated at  $13.65 \text{ keV}$  with a ray-tracing code (Sanchez del Rio & Dejus, 2011; Sanchez del Rio *et al.*, 2011), with figure error and optical thickness variation from grating interferometry taken into account, was: (a) for the  $1 \times 50 \mu\text{m}$  lens,  $148 \mu\text{m} \times 56 \mu\text{m}$ ; (b) for the  $2 \times 100 \mu\text{m}$  lens,  $147 \mu\text{m} \times 57 \mu\text{m}$ . The size calculated for the ideal lens with the same procedure was  $144 \mu\text{m} \times 53 \mu\text{m}$ . The small difference in the focal length can be explained by the fact that the radii of

curvature of the lenses are slightly higher than nominal (see the *Metrology* section). The measured image size exceeds the expected one in both directions for both lenses: in the horizontal by 16% ( $1 \times 50 \mu\text{m}$ ) and 17% ( $2 \times 50 \mu\text{m}$ ), and in the vertical by 9% and 7%, respectively. Simulations show that the lens shape and roughness can change the focal size by only a small amount (3% horizontally, 6% vertically). This suggests that the observed discrepancy (observed mostly in the horizontal direction) predominantly originates from other effects such as the uncertainties in the determination of the source size [typical uncertainties in the evaluation of the source size are about 5% (Vadim Sajaev, private communication)] and/or wavefront distortions due to the upstream beamline optics (thermal slope of the monochromator crystals and imperfections of the Be windows).

#### 4. Conclusions

We have presented the study of beryllium refractive lenses used for X-ray focusing applications, in particular to be used in the future X-ray free-electron laser oscillator sources. Optical metrology reveals that the beryllium lenses have been made accurately to the design specification. X-ray experiments show very encouraging results. Transmissivity of the lenses is >94% for 8 keV and >98% for 14.4 and 18 keV photons. The lenses allow for imaging of the synchrotron radiation X-ray source, with image size exceeded by 16–17% in the horizontal and by 9–7% in the vertical direction when compared with theoretical prediction, however without significant distortions. Single-grating interferometry results indicate that wavefront aberrations caused by the cumulative effect of the surface and bulk inhomogeneities are marginal. The combined results of the metrology and X-ray performance tests allow us to conclude that beryllium lenses are a suitable focusing element for the XFEL setup.

#### Acknowledgements

We thank Albert Macrander for supporting experiments at the 1-BM beamline, Deming Shu for the engineering design of the lens casing, Ruben Reininger for ray-tracing calculation, and Elizabeth Hermans for the editing of the article's text. Work at the Advanced Photon Source was supported by the US Department of Energy, Office of Science, Office of Basic Energy Sciences, under Contract No. DE-AC02-11357.

#### References

Assoufid, L., Shi, X., Marathe, S., Benda, E., Wojcik, M. J., Lang, K., Xu, R., Liu, W., Macrander, A. T. & Tischler, J. Z. (2016). *Rev. Sci. Instrum.* **87**, 052004.  
 Bosak, A., Snigireva, I., Napolskii, K. S. & Snigirev, A. (2010). *Adv. Mater.* **22**, 3256–3259.  
 Byelov, D. V., Meijer, J.-M., Snigireva, I., Snigirev, A., Rossi, L., van den Pol, E., Kuijk, A., Philipse, A., Imhof, A., van Blaaderen, A., Vroege, G. J. & Petukhov, A. V. (2013). *RSC Adv.* **3**, 15670–15677.  
 Chantler, C., Olsen, K., Dragoset, R., Chang, J., Kishore, A. R., Kotochigova, S. & Zucker, D. (2017). *X-ray Form Factor, Attenuation and Scattering Tables* (Version 2.1). National Institute

of Standards and Technology, Gaithersburg, MD, USA. [Online] Available: <http://physics.NIST.gov/ffast>.  
 Chumakov, A. I., Ruffer, R., Leupold, O., Barla, A., Thiess, H., Asthalter, T., Doyle, B., Snigirev, A. & Baron, A. Q. R. (2000). *Appl. Phys. Lett.* **77**, 31–33.  
 Fox, A. G. & Li, T. (1961). *Bell Syst. Tech. J.* **40**, 453–488.  
 Frankot, R. & Chellappa, R. (1988). *IEEE Trans. Pattern Anal. Mach. Intell.* **10**, 439–451.  
 Goodman, J. (2005). *Introduction to Fourier Optics*, 2nd ed. Englewood Cliffs: Roberts & Co.  
 Henke, B. L., Gullikson, E. M. & Davis, J. C. (1993). *At. Data Nucl. Data Tables*, **54**, 181–342.  
 Itoh, H., Nagai, K., Sato, G., Yamaguchi, K., Nakamura, T., Kondoh, T., Ouchi, C., Teshima, T., Setomoto, Y. & Den, T. (2011). *Opt. Express*, **19**, 3339–3346.  
 Kim, K.-J. & Shvyd'ko, Y. V. (2009). *Phys. Rev. ST Accel. Beams*, **12**, 030703.  
 Kim, K.-J., Shvyd'ko, Y. & Reiche, S. (2008). *Phys. Rev. Lett.* **100**, 244802.  
 Kissel, L., Zhou, B., Roy, S., Gupta, S. K. S. & Pratt, R. H. (1995). *Acta Cryst. A* **51**, 271–288.  
 Lengeler, B., Schroer, C. G., Kuhlmann, M., Benner, B., Günzler, T. F., Kurapova, O., Zontone, F., Snigirev, A. & Snigireva, I. (2005). *J. Phys. D*, **38**, A218.  
 Lengeler, B., Schroer, C., Tümmler, J., Benner, B., Richwin, M., Snigirev, A., Snigireva, I. & Drakopoulos, M. (1999). *J. Synchrotron Rad.* **6**, 1153–1167.  
 Macrander, A., Erdmann, M., Kujala, N., Stoupin, S., Marathe, S., Shi, X., Wojcik, M., Nocher, D., Conley, R., Sullivan, J., Goetze, K., Maser, J. & Assoufid, L. (2016). *AIP Conf. Proc.* **1741**, 030030.  
 Marathe, S., Shi, X., Wojcik, M. J., Kujala, N. G., Divan, R., Mancini, D. C., Macrander, A. T. & Assoufid, L. (2014). *Opt. Express*, **22**, 14041–14053.  
 Morgan, A. J., Prasciolu, M., Andrejczuk, A., Krzywinski, J., Meents, A., Pennicard, D., Graafsma, H., Barty, A., Bean, R. J., Barthelmess, M., Oberthuer, D., Yefanov, O., Aquila, A., Chapman, H. N. & Bajt, S. (2015). *Sci. Rep.* **5**, 9892.  
 Polikarpov, M., Snigireva, I. & Snigirev, A. (2014). *J. Synchrotron Rad.* **21**, 484–487.  
 Roth, T., Alianelli, L., Lengeler, D., Snigirev, A. & Seiboth, F. (2017). *MRS Bull.* **42**, 430–436.  
 Sanchez del Rio, M., Canestrari, N., Jiang, F. & Cerrina, F. (2011). *J. Synchrotron Rad.* **18**, 708–716.  
 Sánchez del Río, M. & Dejus, R. J. (2011). *Proc. SPIE*, **8141**, 814115.  
 Schoonjans, T., Brunetti, A., Golosio, B., Sanchez del Rio, M., Solé, V. A., Ferrero, C. & Vincze, L. (2011). *Spectrochim. Acta B*, **66**, 776–784.  
 Schroer, C. G., Kurapova, O., Patommel, J., Boye, P., Feldkamp, J., Lengeler, B., Burghammer, M., Riekel, C., Vincze, L., van der Hart, A. & Küchler, M. (2005). *Appl. Phys. Lett.* **87**, 124103.  
 Schroer, C. G. & Lengeler, B. (2005). *Phys. Rev. Lett.* **94**, 054802.  
 Seiboth, F., Schropp, A., Scholz, M., Wittwer, F., Rödel, C., Wünsche, M., Ullsperger, T., Nolte, S., Rahomäki, J., Parfeniukas, K., Giakoumidis, S., Vogt, U., Wagner, U., Rau, C., Boesenberg, U., Garrovoet, J., Falkenberg, G., Galtier, E. C., Ja Lee, H., Nagler, B. & Schroer, C. G. (2017). *Nat. Commun.* **8**, 14623.  
 Shvyd'ko, Y., Blank, V. & Terentyev, S. (2017). *MRS Bull.* **42**, 437–444.  
 Siegman, A. E. (1986). *Lasers*. Sausalito: University Science Books.  
 Snigirev, A., Kohn, V., Snigireva, I. & Lengeler, B. (1996). *Nature (London)*, **384**, 49–51.  
 Terentyev, S., Blank, V., Polyakov, S., Zholudev, S., Snigirev, A., Polikarpov, M., Kolodziej, T., Qian, J., Zhou, H. & Shvyd'ko, Y. (2015). *Appl. Phys. Lett.* **107**, 111108.  
 Vaughan, G. B. M., Wright, J. P., Bytchkov, A., Rossat, M., Gleyzolle, H., Snigireva, I. & Snigirev, A. (2011). *J. Synchrotron Rad.* **18**, 125–133.  
 Wang, Z., Huang, Z., Zhang, L., Kang, K. & Zhu, P. (2009). *IEEE Trans. Nucl. Sci.* **56**, 1383–1388.